8-1-2017

Effect of Multiphase Radiation on Coal Combustion in a Pulverized Coal jet Flame

Bifen Wu
University of Connecticut - Storrs

Somesh Roy
Marquette University, somesh.roy@marquette.edu

Xinyu Zhao
University of Connecticut - Storrs

Michael F. Modest
University of California, Merced

Accepted version. *Journal of Quantitative Spectroscopy and Radiative Transfer*, Vol. 197 (August 2017): 154-165. DOI.

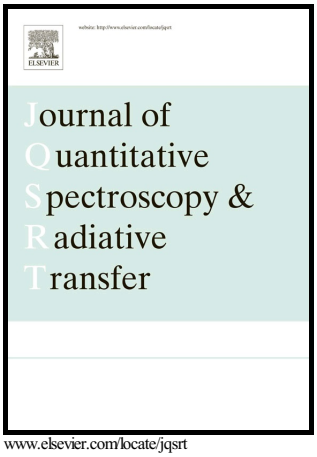

Effect of multiphase radiation on coal combustion in a pulverized coal jet flame

Bifen Wu, Somesh P. Roy, Xinyu Zhao, Michael F. Modest

PII: S0022-4073(16)30595-7
DOI: http://dx.doi.org/10.1016/j.jqsrt.2017.03.017
Reference: JQSRT5627

To appear in: *Journal of Quantitative Spectroscopy and Radiative Transfer*

Received date: 15 September 2016
Revised date: 14 February 2017
Accepted date: 7 March 2017

Cite this article as: Bifen Wu, Somesh P. Roy, Xinyu Zhao and Michael F. Modest, Effect of multiphase radiation on coal combustion in a pulverized coa jet flame, *Journal of Quantitative Spectroscopy and Radiative Transfer*, http://dx.doi.org/10.1016/j.jqsrt.2017.03.017

Effect of multiphase radiation on coal combustion in a pulverized coal jet flame

Bifen Wu[1], Somesh P. Roy[2], Xinyu Zhao[1,*], Michael F. Modest[3]

[1]Department of Mechanical Engineering, University of Connecticut, Storrs, CT 06269, USA

[2]Department of Mechanical Engineering, Marquette University, Milwaukee, WI 53233, USA

[3]School of Engineering, University of California, Merced, CA 95343, USA

bifen.wu@uconn.edu

somesh.roy@marquette.edu

xinyu.zhao@uconn.edu

mmodest@ucmerced.edu

[*]Corresponding Author.

Abstract

The accurate modeling of coal combustion requires detailed radiative heat transfer models for both gaseous combustion products and solid coal particles. A multiphase Monte Carlo ray tracing (MCRT) radiation solver is developed in this work to simulate a laboratory-scale pulverized coal flame. The MCRT solver considers radiative interactions between coal particles and three major combustion products (CO_2, H_2O, and CO). A line-by-line spectral database for the gas phase and a size-dependent nongray correlation for the solid phase are employed to account for the nongray effects. The flame structure is significantly altered by considering nongray radiation and the lift-off height of the flame increases by approximately 35%, compared to the simulation without radiation. Radiation is also found to affect the evolution of coal particles considerably as it takes over as the dominant mode of heat transfer for medium-to-large coal particles downstream of the flame. To investigate the respective effects of spectral models for the gas and solid phases, a Planck-mean-based gray gas model and a size-independent gray particle model are applied in a frozen-field analysis of a steady-state snapshot of the flame. The gray gas approximation considerably underestimates the radiative source terms for both the gas phase and the solid phase. The gray coal approximation also leads to under-prediction of the particle emission and absorption. However, the level of under-prediction is not as significant as that resulting from the employment of the gray gas model. Finally, the effect of the spectral property of ash on radiation is also investigated and found to be insignificant for the present target flame.

Keywords: coal radiation; Monte Carlo; nongray

1. Introduction

Thermal radiation plays a significant role in coal combustion, especially for the emerging new clean coal combustion technologies, such as oxy-coal combustion [1] and combined coal-magneto-hydrodynamics cycle [2]. There either the concentrations of CO_2 and H_2O are high or the overall temperature is elevated. To accelerate the development of such new technologies, an accurate and predictive coal radiation model is necessary. The modeling of radiation during coal combustion is first complicated by its multiphase nature: the particulate media including coal, char and fly ash, emit, absorb, and scatter with different spectral properties. Second, radiatively participative gaseous combustion products, mainly CO_2, H_2O, and CO have spectral properties that are very different from those of the particulate phases. The elevated CO_2 concentration in coal combustion, especially in oxy-coal combustion, can alter the heat transfer pattern from convection-dominant to radiation-dominant [1]. The accumulation of H_2O in coal combustion with wet recycling enhances the possibility of radiation re-absorption as well. Third, unlike other multiphase fuel mixtures such as sprays, coal particles are active emitter due to the combination of high emissivity and high temperature. These aspects of thermal radiation in coal combustion, i.e., propagation of radiation through a particulate medium, the difference between participative gas phase and particulate phase radiative properties, and the emission and absorption by coal particles, have to be considered to accurately model and predict the heat transfer process in coal combustion.

Several radiation solvers, such as the P_N methods [3,4] and the discrete ordinates method [5] have previously been adopted to simulate the coal radiation for their computational expediency. The expensive but accurate Monte Carlo ray tracing (MCRT) method has been applied to combustion applications involving mainly gaseous media [6,7]. In the area of coal combustion, the MCRT method has been applied to solve the radiative transport equation (RTE) [8,9] only recently, due to the recent improvements in computing capabilities. Despite constraints such as

high computational cost and long execution times, the MCRT method has the advantage of reproducing exact solution for sufficiently large statistical samples and the ability to treat inhomogeneous participative media and complex geometries with relative ease. This advantage is crucial for coal radiation modeling because coal combustion often involves both inhomogeneous participative media and complex geometries.

Besides an accurate solver for the RTE, the models for the spectral properties of the coal particles and the gas phase are also crucial for obtaining accurate radiation solutions. Simple gray models are commonly used for coal combustion [10,11]. However, coal, char, fly ash, and the gas phase have distinct spectral properties. Gray models, such as the constant-absorption-coefficient model and the weighted-sum-of-gray-gases model (WSGGM), cannot correctly predict the spectral properties of the mixture without *ad hoc* tuning. Recently, some detailed nongray spectral models are examined in the context of coal combustion [8,12]. Both the full spectrum *k*-distributions model [12] and the line-by-line (LBL) model [9] have been applied to account for the nongray gaseous properties of coal combustion. For coal particles, models that employ large particle limit assumptions [13], as well as the size-dependent Buckius-Hwang correlations [14] are examined in various coal combustion simulations [9,12,15]. To quantify the effects of radiative heat transfer in coal combustion, the present study attempts to bring together the most accurate RTE solver and the most accurate spectral models available for both the gaseous and particle phases. With the increasing computing power, the high-fidelity radiation models become less prohibitive. Therefore, it is a worthwhile exercise to bring the predictive power to the simulation of coal radiation.

The objective of this study is twofold: first, to develop a high-fidelity multiphase MCRT method that accounts for nongray properties of gas and particle phases and second, to investigate effects of nongray spectral properties through parametric studies using a laboratory-scale jet coal flame. In addition to the detailed radiation models, the developed coal combustion solver features a transient Reynolds-averaged Navier-Stokes-based (RANS) Eulerian-Lagrangian multiphase flow solver, a detailed gas-phase chemistry model and the potential of considering turbulence-chemistry-radiation interactions. The flow solver is expected to provide transient information on the number densities of coal particles with reasonable accuracy, which has been found to be essential in predicting the overall effects of radiation [4].

This article is organized as follows. The target flame is introduced in Sec. 2, followed by the description of the physical models and numerical methods in Sec. 3. In Sec. 4, results obtained using the proposed models are presented and discussed, and conclusions are drawn in Sec. 5.

2. The target flame

The target configuration is a laboratory-scale pulverized-coal jet flame. The flame was studied experimentally to investigate the ignition and pyrolysis characteristics of different coal types and coal feed rates [16]. Radiation effects for different size groups of coal particles, as well as lift-off heights and coal burnout rates, were measured in the experiments, for three coal jet flames with different stoichiometric ratios. Only the condition of a stoichiometric ratio of 0.22 is presented in this study where coal particles are injected through a central nozzle with a feed rate of 6.08 mg/s. The Reynolds number of the central jet is approximately 4,400 based on the inlet air viscosity and velocity. Coal particles are ignited by a preheated gas mixture formed by catalytic combustion of propane that contains hot O_2, N_2, CO_2 and H_2O (Table 1). The hot coflow is injected through the square slit as indicated in Fig. 1. The proximate and ultimate analysis of the coal particles used in the experiments are listed in Table 2.

Table 1 Operating conditions.

	Primary jet	Preheated mixture
Average velocity (m/s)	10	4.8
Temperature (K)	300	1,510
Mass fraction (-)		
N_2	0.768	0.761
O_2	0.232	0.101
CO_2	0.0	0.093
H_2O	0.0	0.045

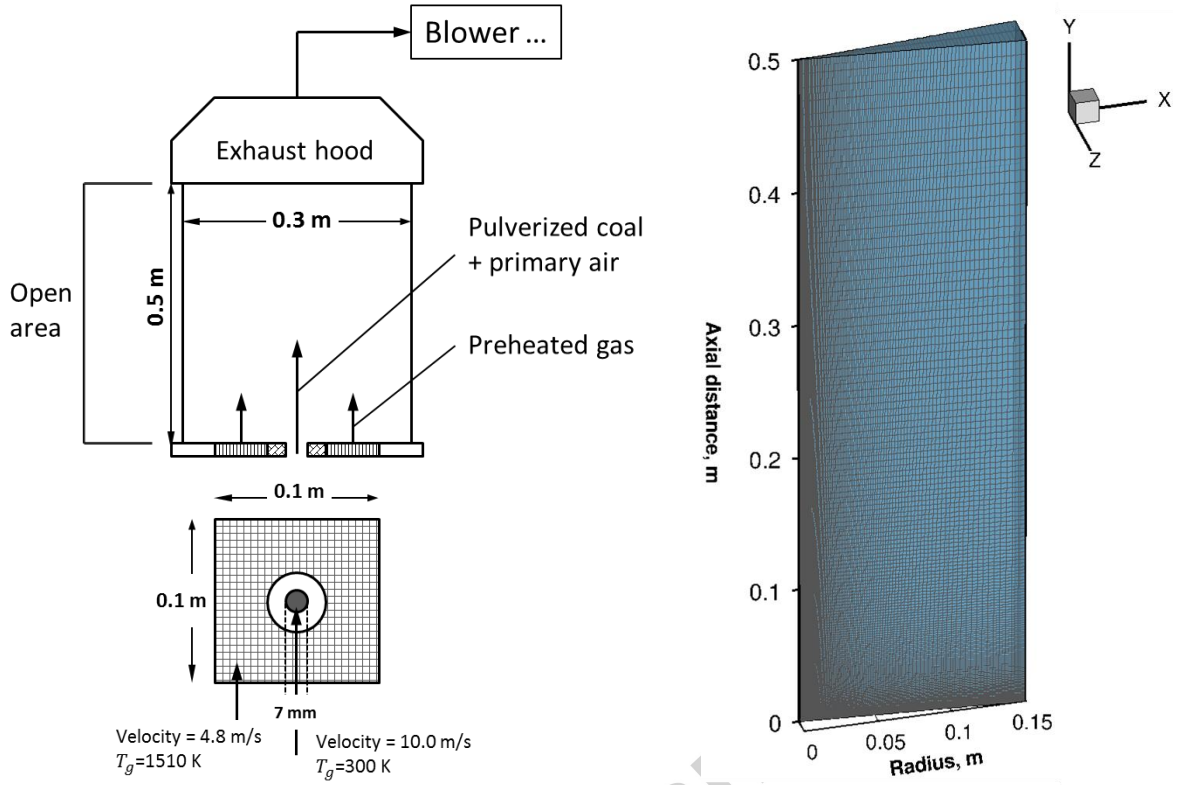

(a) Experimental apparatus (b) Computational domain

Figure 1 A sketch of the experimental setup of the target flame, with details of the inlet jet and the computational mesh.

Table 2 Thermophysical properties of the coal samples.

Parameter	Experimental values	Numerical values
Ultimate analysis (dry-ash-free wt. %)		
C	83.1	83.1
H	4.6	4.6
O	9.9	9.9
N	1.9	2.4
S	0.5	0
Proximate analysis (dry basis wt. %)		
Volatile matter	31.1	31.1
Fixed Carbon	54.0	54.0
Ash	14.9	14.9

The target flame has been the subject of several modeling studies, including both RANS- and large eddy simulation-based (LES) methods [11,15,17]. These simulations show reasonable agreements with the experimental data in some aspects, but also substantial differences in others.

Each simulation has a different focal area, ranging from validating combustion models [15,17] to implementing accurate and inexpensive devolatilization model [11]. It has been postulated in the previous studies that the radiative heat flux is comparable to the convective heat flux after ignition and a better radiation model might improve the accuracy of the prediction of flame lift-off heights.

3. Models and methods

In this section, the models and solution methods are presented. Details on the RTE solver and spectral models will be discussed in Secs. 3.1 and 3.2, respectively, followed by the descriptions of the turbulent multiphase combustion models in Sec 3.3. The remaining numerical details are described in Sec. 3.4.

3.1 The RTE solver

A Monte Carlo ray tracing (MCRT) method is chosen to solve the RTE. The MCRT method can naturally account for the nongray effects of heterogeneous participative media, as well as isotropic/anisotropic scattering. With its stochastic nature, the MCRT method can be easily coupled with other stochastic models to capture turbulence-radiation interactions. Therefore, it is a suitable candidate because the nongray emission/absorption and scattering for the coal-gas mixture are of interest. Instead of directly solving the RTE mathematically, the MCRT method solves radiation transport by emitting and tracking a statistically large number of "energy rays" to account for their interaction with participating media. Each of these energy rays carries a specific amount of energy, and has a specific wavenumber, direction, and origin. They are emitted everywhere within the computational domain. The strength of each energy ray is proportional to the local emission potential of its host cell. The selection algorithms of the origin, propagation direction, and wavenumber of each energy ray are based on random number relations and have been reported in [6,13,18]. As each ray moves through the domain, it loses energy due to absorption by local participating media, and also scatters (i.e., changes direction) according to the scattering potential along its travel path. Each energy ray is tracked until its energy is completely absorbed by the participative media or it hits and/or exits the computational boundaries.

For the multiphase system, the total emission from participating media within the i^{th} finite volume/cell, $Q_{emi,i}$, is equal to the sum of the emission from both the gas and solid phases. The quantity is calculated as

$$Q_{emi,i} = Q_{emi,g,i} + Q_{emi,s,i} \,, \tag{1}$$

where the subscripts g,i and s,i represent gas and solid phases in cell i, respectively. $Q_{emi,g,i}$ and $Q_{emi,s,i}$ are the emission from gas and solid phases on a per-cell basis, respectively,

$$Q_{emi,g,i} = 4\sigma\kappa_{P,g,i}T_{g,i}^4 V_{g,i} \,, \tag{2}$$

$$Q_{emi,s,i} = 4\sigma\kappa_{P,s,i}T_{s,i}^4 V_{s,i} \,, \tag{3}$$

where κ_P, T and V are the Planck-mean absorption coefficient, temperature, and volume of each phase as denoted by the subscript, respectively. The calculation of the Planck-mean absorption coefficients for both the gas and solid phases requires the knowledge of the spectral properties, which will be discussed in Sec. 3.2.

During the tracing of each ray, absorption and scattering are considered as separate discrete events. In the present study, the "energy partition" scheme [19] is adopted for tracking absorption and the amount of energy absorbed by cell i from the k^{th} energy ray emitted from cell j is

$$Q_{abs,ji}^k = Q_{ji}^k\left(1 - \exp\left(-\Delta\tau_{ji}^k\right)\right) \,, \tag{4}$$

where Q_{ji}^k is the energy of the k^{th} ray as it enters the absorbing cell (cell i) and $\Delta\tau_{ji}^k$ is the local optical thickness. If no scattering occurs prior to the departure of the k^{th} energy ray from cell i, the local optical thickness due to absorption of gas and solid phases is computed as

$$\Delta\tau_{ij}^k = \left(\kappa_{g,i} + \kappa_{s,i}\right)S_{ij}^k \,, \tag{5}$$

where S_{ij}^k is the distance traveled by the ray through cell i. With the "energy partition" scheme, the energy of a ray diminishes as it traverses each cell according to

$$Q_{ji}^k = Q_j^k - \textstyle\sum_{i' \in \mathbb{J}_{j(i-1)}^k} Q_{abs,ji'} \,, \tag{6}$$

where Q_{ji}^k is the energy of the k^{th} ray that originated in cell j entering cell i, and Q_j^k is the initial energy of the k^{th} ray, determined by the total emission energy in the j^{th} cell, $Q_{emi,j}$, divided by the number of rays emitted from this cell. The set $\mathbb{J}_{j(i-1)}^k$ denotes all cells crossed by the k^{th} ray emitted from cell j before intersecting cell i.

Isotropic scattering from coal particles is also considered in this study. Scattering only affects the propagation direction of a ray. A collision-based method [13,20] is employed for scattering where the direction of the ray is unaltered until it travels a certain predetermined optical thickness calculated based on scattering coefficient of the participating media along its path. Once the optical thickness due to scattering reaches this threshold, the direction of the ray is altered without changing any other properties.

Once the ray tracing is completed, the radiative source terms can be collected for the gas phase and the solid phase respectively. A Eulerian-Lagrangian system is employed to describe the flow field of the gas and solid phases (described in Sec. 3.3). Therefore, radiative source terms (i.e., absorption - emission) are collected on a per-parcel basis for the Lagrangian coal parcels and they are collected on a per-cell basis for the Eulerian gas phase.

3.2 Radiative properties

The gas phase Planck-mean absorption coefficient is computed as the sum of the Planck-mean absorption coefficient $\kappa_{P,g,m}$ of each individual gas species, i.e.,

$$\kappa_{P,g} = \sum_{m=1}^{M_g} \kappa_{P,g,m} \, , \tag{7}$$

where M_g is the number of participating gas species. For each gas species *m*, individual Planck-mean absorption coefficient is calculated from spectral absorption coefficient based on gas temperature T_g by

$$\kappa_{P,g,m} = \frac{\pi}{\sigma T_g^4} \int_0^\infty \kappa_{\eta,m} I_{b,\eta,m} d\eta \, . \tag{8}$$

The most accurate approach to account for the spectral variation in the gas phase radiative properties is the line-by-line (LBL) approach, which relies on the detailed knowledge of every single spectral line. A LBL database for three major combustion products (CO_2, CO, and H_2O) for temperatures up to 3,000 K is obtained from the HITEMP database to provide spectral properties for the gas phase [21]. A Planck-mean based gray gas model is also tested in this work for the parametric study.

In absence of dependent scattering, the radiative properties of a coal particle (assumed to be a sphere) of radius a are governed by its complex index of refraction, $\boldsymbol{m} = n - ik$, and its size parameter, $x = 2\pi a/\lambda$. The optical properties n and k are the real and imaginary components of the complex index of refraction of the solid particles, and λ is the wavelength. The absorption

and scattering potential of a particle is expressed in terms of efficiency factors for absorption, scattering, and extinction for a particle of radius a, defined as [13]

$$Q_{abs} = \frac{C_{abs}}{\pi a^2}\,,\ Q_{sca} = \frac{C_{sca}}{\pi a^2}\,,\ Q_{ext} = \frac{C_{ext}}{\pi a^2}\,, \tag{9}$$

where C_{abs}, C_{sca}, and C_{ext} are the absorption, scattering, and extinction cross-sections, respectively, and $Q_{ext} = Q_{abs} + Q_{sca}$.

For clouds of particles of non-uniform sizes with the same optical properties, the absorption, extinction, and scattering coefficients are given, respectively, as

$$\kappa_s = \int_0^\infty C_{abs} f(a) da = \pi \int_0^\infty Q_{abs} a^2 f(a) da\,, \tag{10}$$

$$\beta_s = \int_0^\infty C_{ext} f(a) da = \pi \int_0^\infty Q_{ext} a^2 f(a) da\,, \tag{11}$$

$$\sigma_s = \int_0^\infty C_{sca} f(a) da = \pi \int_0^\infty Q_{sca} a^2 f(a) da\,, \tag{12}$$

where the $f(a)$ is the particle size distribution function.

To calculate the radiative properties of coal particles of arbitrary size distribution, we use the Buckius-Hwang correlations [14] that were obtained from a variety of complex indices of refraction and a variety of different particle distribution functions for coal. The Buckius-Hwang correlations present spectral correlations for the absorption coefficient of coal particles in terms of the complex index of refraction and the size parameter. Here, a constant complex index of refraction is assumed in this study, hence the spectral dependence of the complex index of refraction is neglected. However, particles should still be considered as nongray due to their spectrally-dependent size parameters.

To quantify the importance of the nongray effects, the large-particle-limit assumption is also implemented where the extinction, scattering, and absorption efficiencies are not size dependent. Neglecting diffraction, in the large particle limit, the efficiencies can be written as [13],

$$Q_{abs} = \alpha,\ Q_{sca} = \rho,\ Q_{ext} = 1\,, \tag{13}$$

where ρ is the hemispherical reflectance and α is hemispherical absorptance. There, the particles are approximated to be large (i.e., $x \gg 1$) and opaque ($kx \gg 1$), and this is a reasonable assumption for large coal particles (~100 μm) compared to typical mid-infrared wavelength (1 – 10 μm) relevant for combustion. Using Fresnel's relations, the reflectance for unpolarized rays due to normal incidence can be written as [13],

$$\rho = \frac{(n-1)^2 + k^2}{(n+1)^2 + k^2}\,. \tag{14}$$

The values of n and k are indicated in Table 3.

Available data [22] for carbon and different types of coal suggest that the real component of the complex index of refraction, n, varies little over the infrared spectrum and is relatively insensitive to the type of coal. The absorptive index, k, may vary strongly over the spectrum and from coal to coal. Since bituminous coal was used in the experiments, a typical complex index of refraction, $\boldsymbol{m} = 1.85 - 0.22i$ is used for the entire spectral range [8]. Scattering by coal particles is considered to be isotropic when the Buckius-Hwang correlations are used, and is neglected when the large-particle limit is considered.

The composition of the fly ash and its optical properties may also vary greatly from coal to coal. An extensive database exists on the optical properties of ash [22], where there is agreement on a consistent value for the real component of the complex index of refraction (n≈ 1.5) [23]. In contrast, strong wavelength and temperature dependence [23] has been observed for the imaginary component (k) (e.g., from $10^{-4.6}$ to 10^{-1} [22]). In general, there is significant difference in the values of complex index of refraction between coal and fly ash. Therefore, a value of $\boldsymbol{m} = 1.50 - 0.02i$ is chosen for fly ash to study the effect of its presence on radiation characteristics.

During combustion, particles composed of pristine coal or ash rarely exist; most coal particles are partially burnt, especially for the laboratory-scale pulverized coal flames studied here. Therefore, models to calculate the complex index of refraction of partially burnt coal particles are needed. Both linear model and binary-switch model are discussed in literature [23]. A binary-switch model is proposed here, where the complex index of refraction is switched to that of the fly ash when only 5% of the initial mass of the solid carbon remains.

Table 3 The complex indices of refraction for coal and ash used in this study.

Particle Type	$\boldsymbol{m} = n - ik$
bituminous	$1.85 - 0.22i$
fly ash	$1.50 - 0.02i$

Finally, particles of identical diameters are grouped into a computational parcel. It is used to reduce the computational cost of particle tracking. From the computational point of view, parcel and particle are equivalent as long as the projected area for a parcel is scaled with the mass/volume the parcel represents, which is the case in the current model for dilute dispersed phase.

3.3 Chemistry and turbulence models

Detailed kinetic models are used to account for the gas-phase chemical reactions. The coal composition is obtained from the proximate and ultimate analysis as indicated in Table 2. Sulfur is not considered in this study, and the measured amount of sulfur is added to the nitrogen content. The elemental components are distributed among volatile matter, ash, and fixed carbon, according to the proximate and ultimate analysis. By matching the lower heating value to the experimental measurement, the volatile matter is assumed to decompose instantaneously to four small molecules, namely C_2H_4, CO, N_2 and H_2, with mass fractions of 0.307, 0.512, 0.115, and 0.066, respectively. The volatile matter is released from coal particles with a rate determined from Kobayashi's two-rate model [24]. Surface reaction is assumed to occur sequentially after the devolatilization and the global reaction of $C(s) + O_2(g) = CO_2(g)$ is considered as the heterogeneous reaction. A diffusion-kinetic-control surface reaction model [25] is used to determine the heterogeneous reaction rate.

The convective heat transfer for particles is accounted for using the Ranz-Marshall correlation [26]. The specific heat of coal particles is a linear combination of the specific heat of the volatile matter, ash and char. A Rosin-Rammler distribution is employed to describe the initial size distribution of the particles in the coal injection models, and the model parameters are selected based on the experimental measurements.

For the gas phase combustion, the PaSR model [27] is used to calculate the chemical source term, where the model parameter C_ϕ is chosen to be unity, neglecting the effect of turbulent chemistry interaction. A systematically reduced 31-species mechanism [28] is used to model the gas-phase kinetics.

A Reynolds-averaged formulation is used in the simulation in a Eulerian-Lagrangian framework. The gas-phase Favre-averaged continuity, momentum, species, and sensible enthalpy are solved on the Eulerian mesh, and the coal parcels are tracked individually in a Lagrangian manner. Turbulence is modeled using a standard $k-\varepsilon$ model [29] with a modified constant $C_{\varepsilon 1} = 1.6$. A two-way coupling scheme that accounts for mass, momentum and energy transfer between the gas phase and coal particles is considered. The mean source terms originating from the coal particle motion and reaction are collected in a particle-source-in-cell manner (PSIC) [30].

3.4 Computational domain and numerical details

The coupled mean continuity, mean momentum and turbulence equations are solved using a structured finite-volume method with a second-order spatial discretization and a first-order time discretization scheme in OpenFOAM-2.2.x [31]. The radiative heat transfer models are implemented in separate FORTRAN codes and coupled with OpenFOAM.

The computational mesh employed in this study is a 10° axisymmetric wedge consisting of 15,000 hexahedral cells for computational expediency. The wedge-like 3D grid [31], shown in Fig. 1, is one-cell thick in the azimuthal direction. The grid is refined in the mixing regions near the inlet to resolve the mixing layer between the fuel jet and the preheated mixture, and is stretched in the coflow and downstream to save computational time. 100,000 parcels are injected per second, and 5,000 to 6,000 parcels are present at every time step within the computational domain after the flame reaches statistically stationary state. Constant pressure boundary condition and zero gradient condition for all other scalars are applied at the outlet and at the outer peripheral boundary. For velocity, a fixed value of 0.16 m/s along the radial direction is prescribed for the outer peripheral boundary to account for the entrained flow rate resulting from the exhaust fan [11]. Buoyancy effects are considered as per direction of gravity in the experimental setup. Symmetry conditions are applied at the two lateral faces.

Table 4 Baseline physical models and numerical parameters for the target flame.

Item	Model	Baseline values
Eulerian CFD	Structured finite-volume method	Axisymmetric, 15,000 cells
Turbulence closure	standard $k-\varepsilon$	$C_\mu = 0.09$, $C_{\varepsilon 1} = 1.60$, $C_{\varepsilon 2} = 1.92$, $\sigma_k = 1.0$, $\sigma_\varepsilon = 1.3$
Gas phase chemistry	31-species detailed mechanism	-
Devolatilization	Two-rate model	$A_1 = 2.0 \times 10^5$ 1/s, $\alpha_1 = 0.3$, $E_1 = 1.05 \times 10^8$ J/kmol K, $A_2 = 1.3 \times 10^7$ 1/s, $\alpha_1 = 1.0$, $E_2 = 1.67 \times 10^8$ J/kmol K
Surface reaction	Diffusion-kinetic-control model	$A = 0.011$ (kg/m^{2}s) (N/m^2), $E = 5.0 \times 10^7$ J/kmol K, $S_b = 1.0$
Coal properties	Constant volume, constant char and ash specific heat	$C_{p_{char,ash}}$ = 710 J/kg K 100,000 parcels per second
Convective heat	Ranz-Marshall	-

transfer	correlation	
Dispersion	Stochastic dispersion model	-

A summary of the models used in the baseline case is provided in Table 4. A gas phase mixing simulation is first performed to obtain fully-developed flow and temperature fields. No combustion or radiation is involved during this stage. The coal particles are then injected after approximately ten flow-through times, while the injection duration is about twenty flow-through times, based on the fuel jet inlet. Finally, the coal combustion is performed for ten flow-through times until a statistically stationary state is reached. Statistics are collected over another ten flow-through times.

Table 5 A summary of the conditions of the test cases.

	Solid phase	Gas phase
Case 1	Baseline (N/A)	Baseline (N/A)
Case 2	Large (OT)	Gray (OT)
Case 3	BH correlations (OT)	LBL (OT)
Case 4	BH correlations	LBL
Case 5	Large (OT) with ash properties	Gray (OT)

The test cases with different combinations of radiation models are summarized in Table 5. Results obtained from these test cases are compared in Sec 4. In Table 5, "Large" represents the large particle limit, and "BH correlations" denotes cases using the Buckius-Hwang correlations. "LBL" represents the line-by-line spectral model, and "Gray" denotes the gray gas model. "OT" represents optically thin radiation model, where no absorption is considered. The baseline case is a simulation without any radiation model.

4. Results and Discussion

The baseline (Case 1) results for the target flame are shown first in this section followed by results obtained from the optically thin (OT) simulations (Case 2 and 3) and the nongray simulation (Case 4). The effects of nongray radiation on the evolution of coal particles are examined next. Following that, parametric studies of the nongray effects are performed. Finally, the effect of different ash properties is briefly explored.

4.1 Baseline model results

Figure 2 shows the mean mass fractions of radiatively important gaseous species for Case 1. To demonstrate the effect of combustion, the minimum values of CO_2 and H_2O are set to be their corresponding inlet levels in the hot preheated mixture. CO_2 can be produced by two processes: the complete combustion of volatile matters (CO and C_2H_4) and the surface reaction. The oxidation of volatile matters leads to a CO_2-rich zone between 0.1 m and 0.2 m downstream the inlet, while the surface reaction creates a second CO_2-rich zone further downstream, as indicated in Fig. 2. Water vapor is produced only through the combustion of volatile matter (e.g., C_2H_4 and H_2). Therefore, water vapor starts to form between 0.1 m and 0.2 m and begins to decline towards the exit of the domain because the devolatilization process is almost completed there. As a major pollutant, CO is formed through devolatilization and partial combustion, and is eventually consumed through oxidation. Therefore, its concentration peaks at locations where the O_2 concentration is relatively low and where the devolatilization is still active. It should be noted that the peak mass fraction of CO is comparable to that of H_2O.

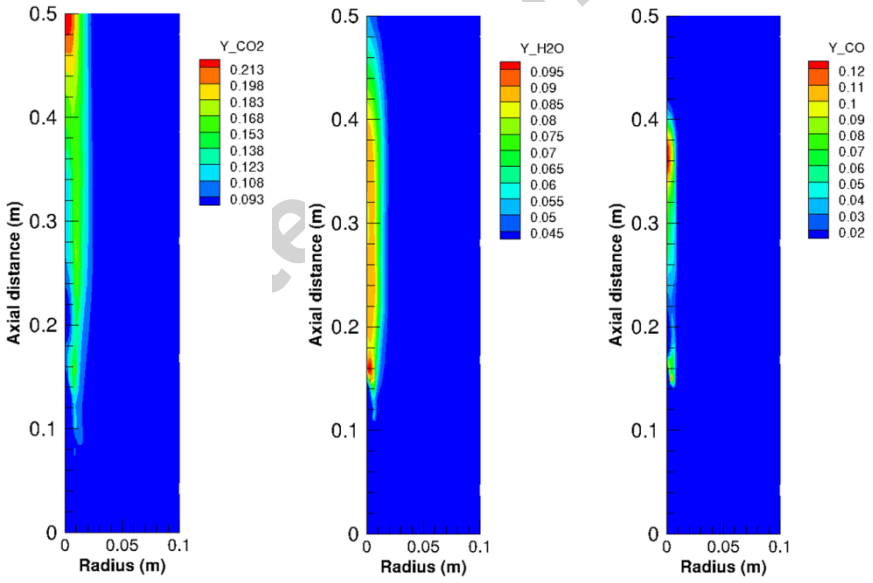

(a) CO_2 (b) H_2O (c) CO

Figure 2 Mass fraction contours obtained from Case 1 for (a) CO_2, (b) H_2O, and (c) CO.

The lift-off height of the test flame is one of the key observables reported by the experimental study. A high-speed camera was used to capture the flame development in the experiment. Three distinct flame regions were identified from the experiment [16]: isolated bright particles (IBP), the growing flame (GF) and the continuous flame (CF). Ignited particles in

the IBP region are isolated and do not contribute to the growth of the flame. In the GF region (0.15 m to 0.2 m), the ignited cloud is growing and eventually the CF region takes shape in which the center of the jet is combusting stably. Consequently, the lift-off height of the coal flame can be defined as the bottom of the CF region (which is fluctuating in space). As a second definition, the lift-off height can be defined as the axial position where the local mean gas temperature first exceeds 1,560 K [11]. Using the second definition, the lift-off height of the target flame is approximately 0.12 m, which is lower than the experimental observation. The competing effects of radiative heat loss from the hot products and the radiation gain of coal particles near the inlet can alter the lift-off height of the test flame, which is discussed in Secs. 4.3 and 4.4.

4.2 Optically-thin simulations: maximum impact of radiation

Case 2 is simulated as a limiting condition where maximum possible temperature difference resulting from considering radiation can be observed. Figure 3 compares the temperature field obtained from Cases 1 and 2. As expected, the computed peak mean temperature is lower when a gray, optically thin model is used. The maximum decrease of the mean temperature is greater than 500 K near the outlet, as shown in Fig. 3(c). It should be noted here that the flame structure changes significantly when considering radiation. Comparison solely based on same physical locations might not reveal all the factors that cause the observed difference.

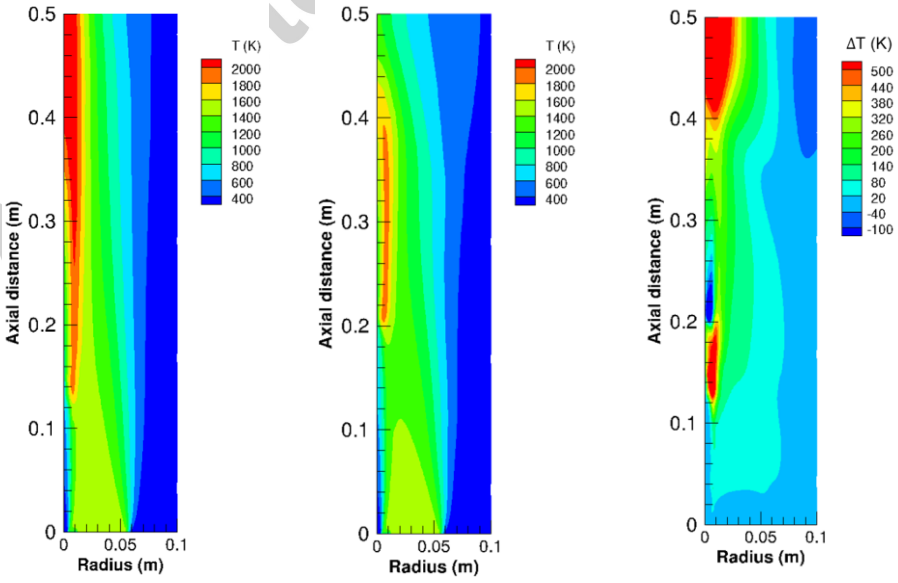

(a) Case1 (b) Case 2 (c) ΔT

Figure 3 Temperature contours obtained from (a) Baseline (Case 1) and (b) Large/Gray (OT) (Case 2). Subfigure (c) shows the difference in temperature, ΔT = Case 1 – Case 2.

The gas phase emission predicted in Case 2 is presented in Fig. 4(a), while the logarithm of the ratio of the coal emission to gas phase emission is shown in Fig. 4(b). It is found that the heat loss due to coal emission is dominant in the jet core due to the stronger radiative effect of coal particles, which is an order of magnitude higher than the gas phase emission. Emission from the gas phase is comparable to coal emission outside the injection core, and becomes more important in the pure coflow stream. Case 3 is also simulated here where nongray properties are used for both the gas and solid phase. No discernible difference can be observed because only emission is considered in Cases 2 and 3. It should be noted that the computational cost associated with Case 2 is an order of magnitude lower than that of Case 4 (shown in Sec. 4.3) because no RTE is solved. Due to its computational expediency, Case 2 is used as a test-bed for further parametric studies shown in later sections.

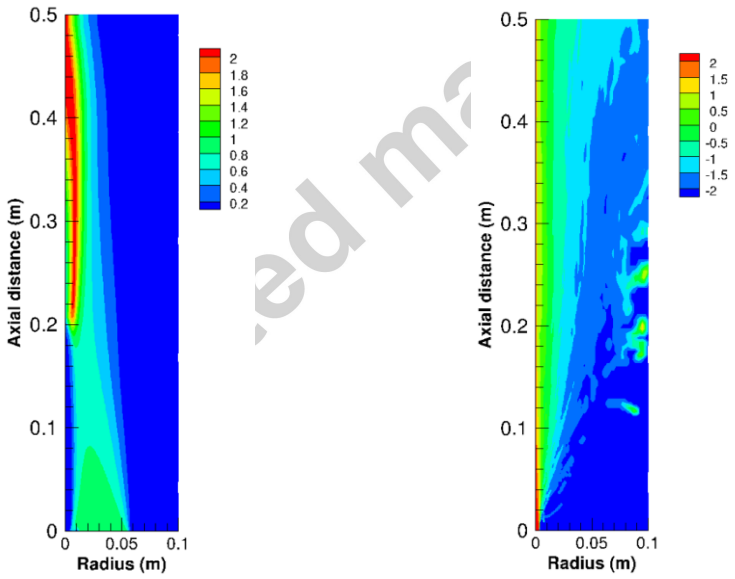

(a) Gas emission (b) Logarithm of the ratio of coal-to-gas emission

Figure 4 Radiative emissions obtained from Case 2: (a) Gas emission (MW/m^3), and (b) logarithm of ratio of coal emission to gas emission.

4.3 Nongray simulation with emission and re-absorption

Case 4 is used to demonstrate the thermal radiation effect when considering both emission and re-absorption. This is the most accurate and detailed combination of models. The lift-off heights are first compared between the experiment and the simulations for both Case 1 and Case

4, as shown in Fig. 5. As a reference, we also include the 1,560 K isoline (black line) in Fig. 5. The flame is lifted higher when radiation is considered according to both definitions of the lift-off height. Approximately 35% increase in the lift-off height is observed for Case 4 compared to Case 1, according to the second definition of the lift-off height. Overall, by considering radiation, the heating rate of the coal particles is reduced, which leads to delayed devolatilization and ignition. Due to the difference in ignition characteristics, the flame structure is altered.

Radial profiles of gas phase temperature at four downstream locations are compared in Fig. 6. Due to the dominance of the emission from preheated gas and absorption by coal particles near the inlet at H=0.05 m, the gas phase temperature is lower when radiation is considered. From H=0.25 to 0.35 m, the strongly burning flame becomes dominant, and the difference in the gas phase temperature can reach up to 500 K. At H = 0.45 m, the difference in the gas phase temperature becomes much larger than at upstream locations due to the change of flame structure and the radiative heat loss from the hot heterogeneous mixture. The tight coupling between the chemical reactions and the temperature leads to a significantly altered species concentration field, which in turn changes the radiative spectral properties of the gas phase.

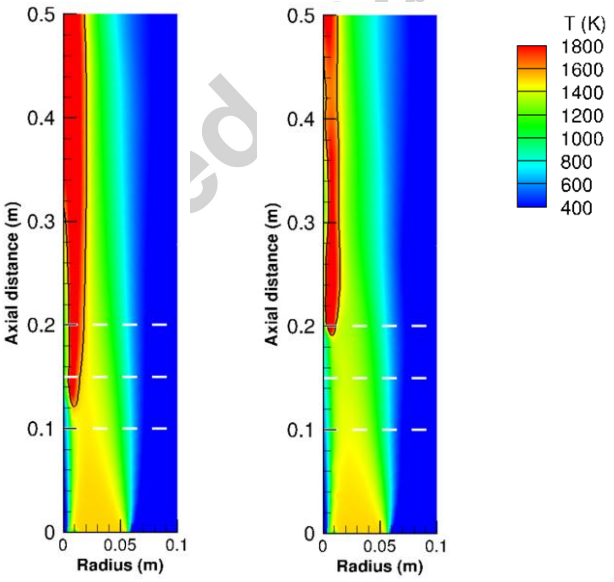

(a) Case 1 (b) Case 4

Figure 5 Temperature contours obtained from (a) Baseline (Case 1) and (b) BH/LBL (Case 4) for measurement of the lift-off height. The black line is the isoline of T = 1,560 K (i.e., the second definition of lift-off height [11]). The white dashed lines mark 0.1 m, 0.15 m, and 0.2 m downstream, respectively.

The indirect effect of radiation on convective heat exchange between the gas phase and particle phase is explored in Fig. 7, where the red dots denote convective heat transfer from gas to particle and the blue dots denote convective heat transfer from particle to gas. As shown in Fig. 7, heat is transferred from the gas to the particle phases mainly through convection for both cases before the lift-off height (approximately 0.2 m). The direction of convective heat transfer reverses (i.e., from particle to gas) for most of the particles in the baseline (Case 1) due to the higher particle temperature. However, in Case 4, beyond the lift-off height, radiation reduces particle temperature dramatically and hence the direction of convective heat transfer remains to be from gas to particles throughout the flame for a significant amount of particles. Also noticeable from Fig. 7 is the substantial drop in particle temperature near the exit boundary when nongray radiation is considered.

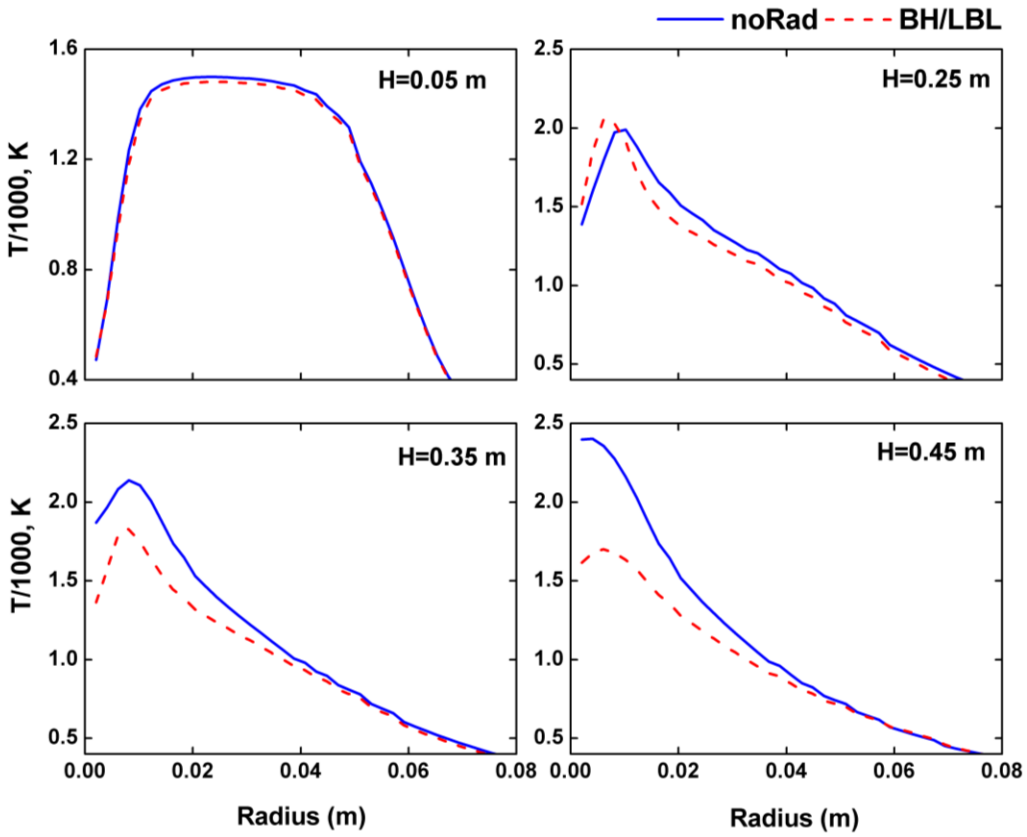

Figure 6 Radial profiles of the gas phase temperature obtained from Case 1 (blue solid line) and Case 4 (red dashed line). Temperature is scaled by 1000.

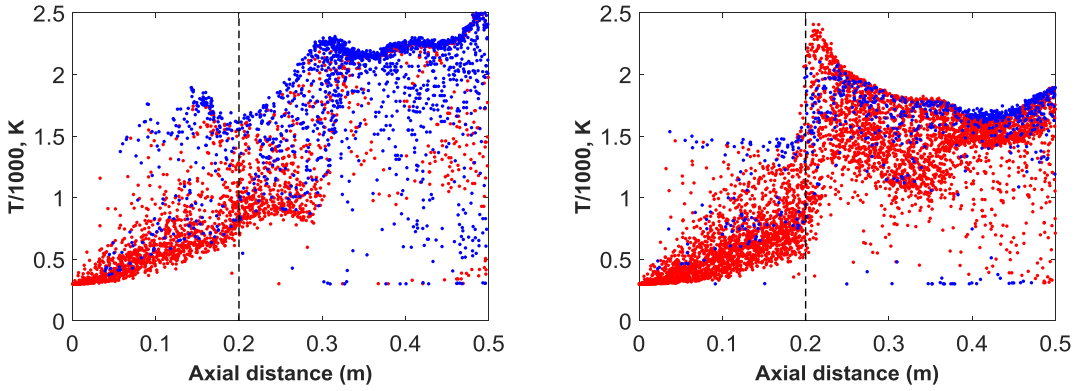

(a) Case 1 (b) Case 4

Figure 7 Scatter plots of particle temperature distribution along the axial direction. Each dot represents a coal parcel. Red dots denote convection of heat from gas to the particle and blue dots denote convection of heat in the opposite direction. Temperature is scaled by 1000.

4.4 Effects of radiation on the particle evolution

Effects of radiation on the dynamics of coal particles are investigated by tracking 110 coal parcels that are injected approximately at the same time (i.e., within a span of 1.5×10^{-4} s after attaining the statistically stationary state) and approximately at the same location (i.e., within 0.015 m from the inlet in the axial direction). These parcels are then classified into three groups based on their diameters, d: $d \in (0, 30]$ μm, $d \in (30, 70]$ μm and $d > 70$ μm. The radiation-to-convection ratio, ϕ_{rc}, which is an important indicator of the heat transfer mechanism for the solid phase, is defined as:

$$\phi_{rc} = \left| \frac{S_{radp}}{S_{convp}} \right|, \tag{15}$$

where S_{radp} and S_{convp} are the Lagrangian radiation source and convection source for a given coal particle, respectively.

Figure 8(a) shows the evolution of ϕ_{rc} along the axial direction for the three groups. Each dot in Fig. 8 represents a parcel. The horizontal dashed line represents the value of unity, and the vertical dashed line marks the lift-off height obtained using the second definition. Before the lift-off height, convective heat transfer is dominant for all size groups. The parcels with stronger radiation effects mostly belong to the small particle size group due to the relatively higher temperature for small particles (Fig. 8(b)) in this region. After the parcels move beyond the lift-off height, radiation becomes equally or more important compared to convection for all three

groups as indicated by the red dots that are populated in the top-right zone. By collecting the probability density functions of ϕ_{rc} for all three size groups (not shown here) in the top-right zone of Fig. 8(a), it can be observed that radiation plays a more significant role than convection for the medium and large particles, which is consistent with the experimental observations in [16].

The temperature evolution for parcels from different size groups is plotted in Fig. 8(b). Two peaks are observed for small particles. The first peak is due to the volatile matter combustion, and the second peak is caused by the surface reaction. The temperature of medium and large particles increases slowly before the lift-off height, due to their relatively larger heat capacity. To investigate the completeness of particle burning, Fig. 8(c) shows the burnout rate, which is defined as

$$B = 1 - \frac{M_{C,r}}{M_{C,i}}, \tag{16}$$

where $M_{C,r}$ and $M_{C,i}$ denote the remaining and the initial combustible matter (volatile matter plus solid carbon), respectively, in the parcel.

Two-stage burnout is observed for all particles, with the first stage caused by the fast devolatilization and the second stage caused by the relatively slower surface reaction. The characteristics of the two stages are different for different particle size groups. Smaller particles burn out faster because they respond faster to heating. Most of the medium-to-large particles burn out near the outlet, while many small particles complete burning before reaching the continuous flame indicated by the lift-off height.

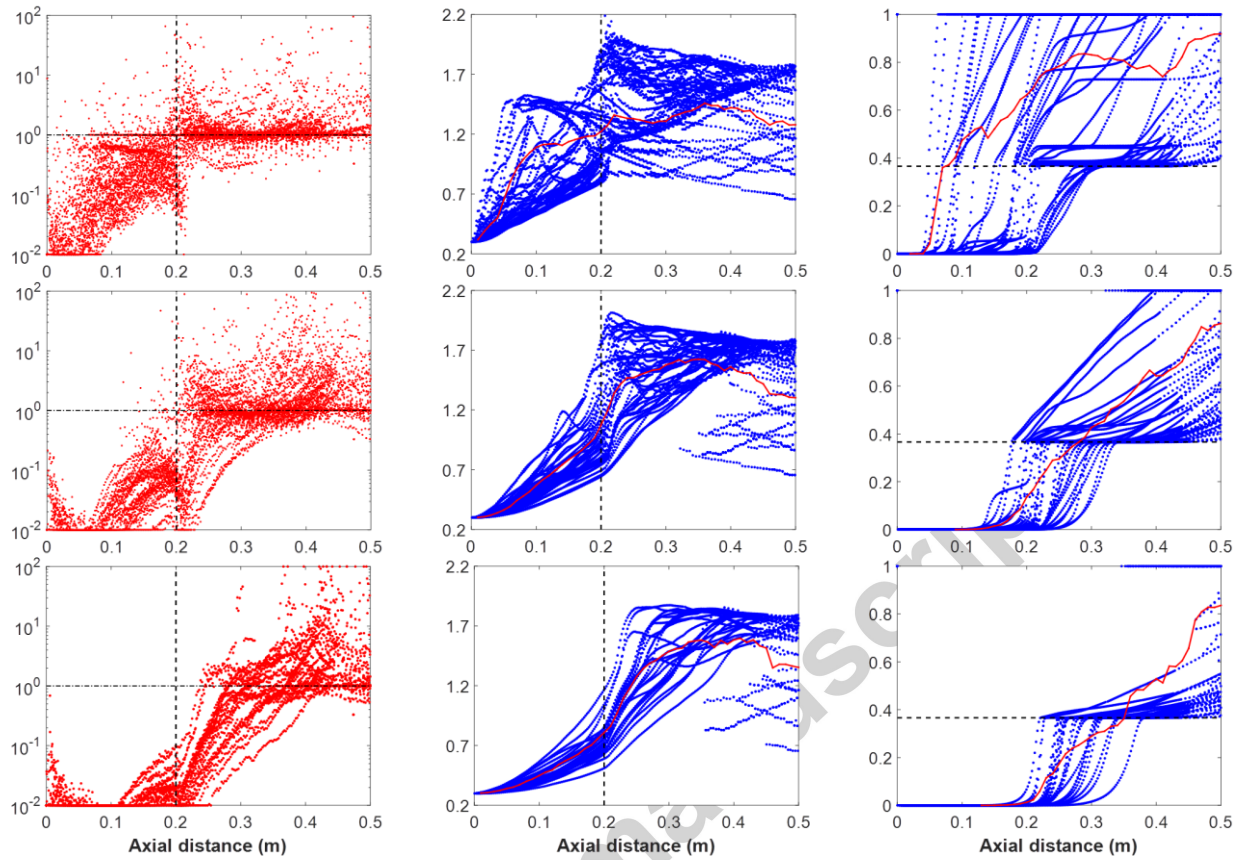

(a) ϕ_{rc}(-) (b) T/1000, K (c) B(-)

Figure 8 Radiation-to-convection ratio, temperature, and burnout rate history for 110 coal parcels along the axial direction. The first, second, and third row represent groups of small, medium, and large particles as defined in the text, respectively. The red solid lines represent the mean temperature and burnout rate for each group. Temperature is scaled by 1000.

4.5 Effects of the nongray spectral properties

A frozen-field analysis is conducted here to demonstrate the effects of nongray spectral properties. Since unsteady RANS with Lagrangian particles were used in the simulation, the statistically steady state snapshot was obtained after time-marching the simulation for a large amount of time steps. The temperature and species concentration fields obtained from the solution of Case 2 are analyzed. The MCRT simulations were run for a sufficient number of iterations to obtain a statistically converged solution. The standard deviation of the solution is small enough and, hence, is not shown in the line plots for clarity. The cases considered are: i) gray gas with large (gray) particle approximation, referred to as *Set-GG* hereinafter; ii) LBL gas

with large (gray) particle approximation, referred to as *Set-NGG* hereinafter; and iii) LBL gas with BH correlation for particles (nongray), referred to as *Set-NGNG* hereinafter.

The impact of nongray gas-phase properties is first evaluated by comparing results obtained using *Set-NGG* and *Set-GG*. Figure 9(a) presents the radial distributions of the absorption by gas at three axial locations. The absorption by gas using the models *Set-NGG* is significantly higher than that from the models *Set-GG*, as evident in Fig. 9(a). To clearly present the difference in the absorption source terms for coal, the relative difference between absorption source terms for coal obtained from *Set-NGG* and from *Set-GG*, θ, is defined as

$$\theta = \frac{Q_{Set-NGG} - Q_{Set-GG}}{Q_{Set-NGG}}, \tag{17}$$

where Q denotes the absorption terms of the coal particles obtained using the models indicated by the corresponding subscript. Using models *Set-GG*, the solid phase absorption is predicted to be higher than that obtained using models *Set-NGG* for all three locations. Largest difference can be observed at location H=0.35 m where a significant amount coal parcels are available with high temperatures.

The effects of nongray particle spectral models are examined next. Figure 10 compares results obtained from models *Set-NGG* with those obtained from models *Set-NGNG*. The gas phase absorption is slightly lower (approximately 20%) when gray models are employed for coal. For coal particles, the emission and absorption source terms obtained from *Set-NGG* are also slightly lower than those obtained from *Set-NGNG*. By comparing Figs. 9 and 10, it can be seen that the employment of non-gray gas phase spectral models makes a larger difference than the employment of non-gray solid-phase spectral models in terms of source term prediction.

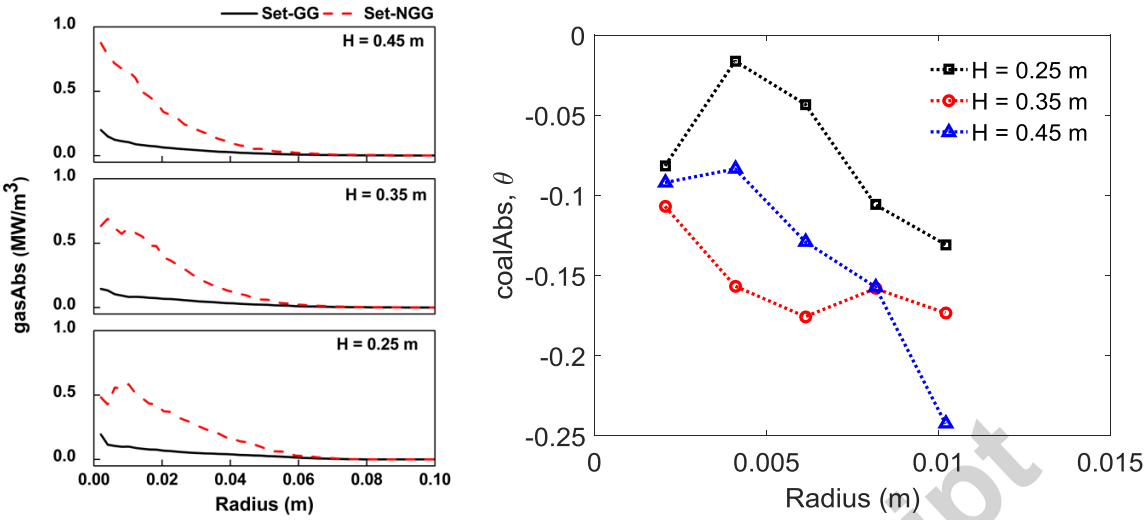

(a) Gas absorption (b) Relative difference of coal absorption

Figure 9 Effects of nongray and gray gas approximations on (a) absolute values of gas absorption and (b) relative differences of coal absorption (θ) at three downstream locations. Frozen field is based on the steady state solution obtained from Case 2.

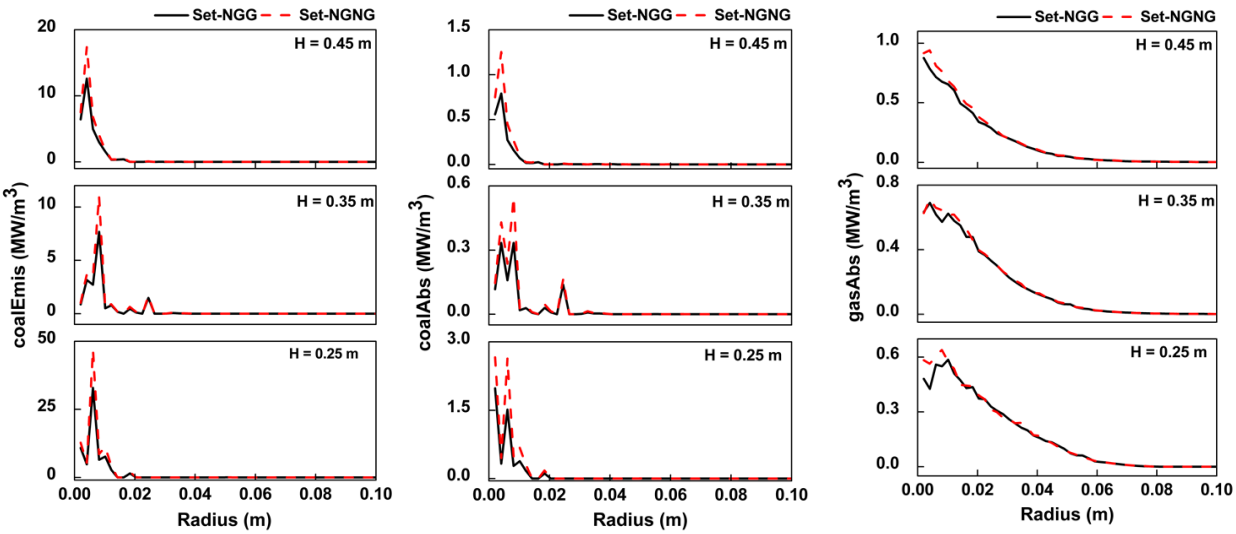

(a) Coal emission (b) Coal absorption (c) Gas absorption

Figure 10 Effects of nongray and gray particles approximations on (a) coal emission, (b) coal absorption, and (c) gas absorption. Frozen field is based on the steady state solution obtained from Case 2.

4.6 Effects of the different spectral properties of ash

Both a linear model and a binary switch model are tested using the 1-D validation condition described in Appendix A.1. No significant difference is observed for the test flame when the spectral property of ash is considered because of the low loading rate and the small burnout rate of coal particles inside the open flame system. It has been found that no significant change is observed in the convective heat flux or divergence of radiative flux distributions when the ash is up to 0.0005 kg/m^3 [4]. The effect of fly ash is prominent in furnace combustion where the coal burnout rates are higher and the deposition of fly ash on the furnace walls is significant [3].

5. Conclusions

A Monte Carlo ray tracing radiative heat transfer solver is developed to study the radiative characteristics in turbulent coal combustions. The developed solver incorporates detailed radiative spectral properties for both the gas (LBL) and solid phases (Buckius-Hwang correlations). The MCRT-LBL/BH solver is coupled with a full Reynolds-averaged Navier-Stokes based turbulent multiphase combustion solver to solve the coupled turbulent-coal-combustion-radiation problem. A laboratory-scale pulverized coal flame is chosen as the target flame, for which experimental measurements are available. A set of test cases are developed to study the effects of radiative heat transfer in coal combustion. Parametric studies are also performed to quantify the significance of the nongray effects for both the gas and solid phases.

It has been found that an over-prediction of more than 500 K in temperature can be observed when neglecting radiative heat transfer. This large difference can alter the lift-off heights, flame shapes, temperature fields, as well as species concentration fields. By tracking coal parcels that originate from the same location and the same time, the different responses of the coal particles within different size groups are compared. Small particles ($d \in (0, 30]$ μm) ignite and burn out faster than medium and large parcels, and they contribute to the ignition of the coal clouds significantly. The ratio of radiative heat transfer source and the convection heat transfer source for individual parcel shows that radiation tends to be more dominant for medium size parcels ($d \in (30, 70]$ μm) compared to the other size groups, which is consistent with experimental observations. Parametric studies of the nongray effects are carried out through the frozen-field analysis based on the steady state solution obtained from Case 2. With the coal particles kept as gray, switching between nongray and gray gas-phase models create significant differences in the

emission and absorption source terms. Meanwhile, with the gas phase kept as nongray, switching between nongray and gray solid-phase models results in less significant differences. This is partly due to the fact that the particle loading rate is low and the residence time is short in the test flame. It is expected that the nongray effects from both the gas phase and the solid phase will be more prominent in furnace-like configurations. Future work includes the incorporation of the effects of anisotropic scattering for heavy particle loading conditions. Studies on the effect of turbulence-chemistry-radiation interactions and larger-scale oxy-coal furnace simulations are also planned for the future.

Acknowledgements

This work was partly supported through the startup fund of Prof. Xinyu Zhao at University of Connecticut. The second and fourth authors would like to acknowledge NSF/DOE for the Collaborative Research Award No. 1258635 and the AFOSR for Contract No. FA8650-15-C-2543. This work used the Extreme Science and Engineering Discovery Environment (XSEDE), which was supported by National Science Foundation grant number ACI-1053575.

Appendix

A.1 Validation of the MCRT method in a one-dimensional slab

The MCRT scheme is validated in a one-dimensional slab, where exact solutions to the RTE can be obtained. The slab is bounded by two cold black walls 0.1 m apart. Coal particles are distributed in the finite volume cells in a way that a desired spatial distribution of bulk Eulerian coal absorption coefficient can be obtained. All particles are identical and have a diameter of 5 μm. The number of particles per computational cell was adjusted to obtain a constant distribution of $\kappa_d = 70$ m^{-1}. The gas mixture was chosen to have a homogeneous distribution with an absorption coefficient of $\kappa_g = 30$ m^{-1}. All properties were assumed to be gray. Two cases were investigated. In both cases gas temperature was kept at constant 2000 K. In the first case the coal particles were assumed to be cold, i.e., nonemitting, and in the second case they were assumed to be at the same temperature of gas (2000 K). The results for the total radiative heat source as well as that for individual phases are shown in Fig. A1. The exact solution is also given in the same

figure. In both cases, the results obtained from the MCRT calculation agree well with the analytical solutions.

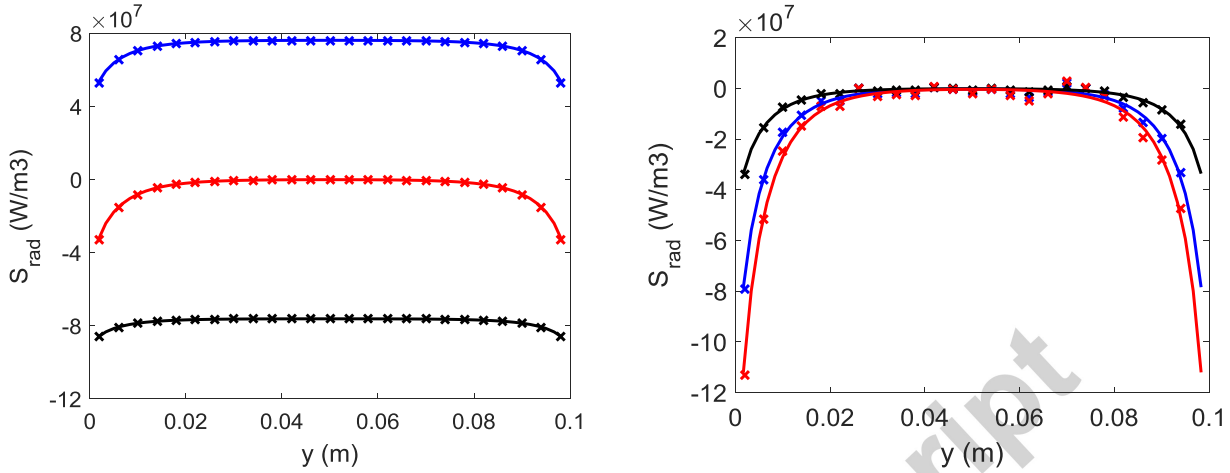

(a) Hot gas/ cold particle (b) Hot gas/ hot particle

Figure A1. Comparison of radiative heat source for a one-dimensional slab with homogeneous media. The solid lines and symbols represent exact solutions and MCRT solutions, respectivly, for particle radiation source terms (blue), total radiation source terms (red), and gas radiation source terms (black).

References

[1] Smart JP, O'nions P, Riley GS. Radiation and convective heat transfer, and burnout in oxy-coal combustion. Fuel 2010;89:2468–76.

[2] Kayukawa N. Open-cycle magnetohydrodynamic electrical power generation: a review and future perspectives. Prog Energy Combust Sci 2004;30:33–60.

[3] Marakis JG, Papapavlou CH, Kakaras E. A parametric study of radiative heat transfer in pulverised coal furnaces. Int J Heat Mass Transfer 2000;43:2961–71.

[4] Varma KR, Mengüç MP. Effects of particulate concentrations on temperature and heat flux distributions in a pulverized-coal fired furnace. Int J Energy Res 1989;13:555–72.

[5] Chen L, Yong SZ, Ghoniem AF. Oxy-fuel combustion of pulverized coal: characterization, fundamentals, stabilization and CFD modeling. Prog Energy Combust Sci 2012;38:156–214.

[6] Wang A, Modest MF. Photon Monte Carlo simulation for radiative transfer in gaseous media represented by discrete particle fields. J Heat Transfer 2006;128:1041–9.

[7] Zhao X-Y, Haworth DC, Huckaby ED. Transported PDF modeling of nonpremixed turbulent $CO/H_2/N_2$ jet flames. Combust Sci Technol 2012;184:676–93.

[8] Cai J, Handa M, Modest MF. Eulerian-Eulerian multi-fluid methods for pulverized coal flames with nongray radiation. Combust Flame 2015;162:1550–65.

[9] Marquez R, Modest MF, Cai J. Spectral photon Monte Carlo with energy splitting across phases for gas–particle mixtures. J Heat Transfer 2015;137:121012.

[10] Kühlert K, Renz U. A comprehensive radiation model for numerical simulations of pulverised coal flames. Heat Transfer 1998 Proc 11 Int Heat Transfer Conf 1998:23–8.

[11] Yamamoto K, Murota T, Okazaki T, Taniguchi M. Large eddy simulation of a pulverized coal jet flame ignited by a preheated gas flow. Proc Combust Inst 2011;33:1771–8.

[12] Yu MJ, Baek SW, Kang SJ. Modeling of pulverized coal combustion with non-gray gas radiation effects. Combust Sci Technol 2001;166:151–74.

[13] Modest MF. Radiative heat transfer. Third Edit. Academic press; 2013.

[14] Buckius RO, Hwang DC. Radiation properties for polydispersions: application to coal. J Heat Transfer 1980;102:99–103.

[15] Zhao X-Y, Haworth DC. Transported PDF modeling of pulverized coal jet flames. Combust Flame 2014;161:1866–82.

[16] Taniguchi M, Okazaki H, Kobayashi H, Azuhata S, Miyadera H, Muto H, et al. Pyrolysis and ignition characteristics of pulverized coal particles. J Energy Resour Technol 2001;123:32–8.

[17] Taniguchi M, Yamamoto K, Okazaki T, Rehfeldt S, Kuhr C. Application of lean flammability limit study and large eddy simulation to burner development for an oxy-fuel combustion system. Int J Greenh Gas Control 2011;5:S111–9.

[18] Ren T, Modest MF. A hybrid wavenumber selection scheme for line-by-line photon Monte Carlo simulations in high-temperature gases. J Heat Transfer 2013;135:84501.

[19] Modest MF. Three dimensional radiative exchange factors for nongray, nondiffuse surfaces. Numer Heat Transfer, Part B 1978;1:403–16.

[20] Howell RJ. The Monte Carlo Method in Radiative Heat Transfer. J Heat Transfer 1998;120:547–60.

[21] Rothman LS, Gordon IE, Barber RJ, Dothe H, Gamache RR, Goldman A, et al. HITEMP, the high-temperature molecular spectroscopic database. J Quant Spectrosc Radiat Transfer 2010;111:2139–50.

[22] Im KH, Ahluwalia RK. Radiation properties of coal combustion products. Int J Heat Mass Transfer 1993;36:293–302.

[23] Goodwin DG, Mitchner M. Flyash radiative properties and effects on radiative heat transfer in

coal-fired systems. Int J Heat Mass Transfer 1989;32:627–38.

[24] Kobayashi H, Howard JB, Sarofim AF. Coal devolatilization at high temperatures. Symp Combust 1977;16:411–25.

[25] Baum MM, Street PJ. Predicting the combustion behaviour of coal particles. Combust Sci Technol 1971;3:231–43.

[26] Ranz WE, Marshall WR. Evaporation from drops: Part 1 and 2. Chem Eng Prog 1952;48:141–7, 173–80.

[27] Nordin PA. Complex chemistry modeling of diesel spray combustion. Chalmers University of Technology; 2001.

[28] Mehta RS, Haworth DC, Modest MF. An assessment of gas-phase reaction mechanisms and soot models for laminar atmospheric-pressure ethylene–air flames. Proc Combust Inst 2009;32:1327–34.

[29] Launder BE, Sharma BI. Application of the energy-dissipation model of turbulence to the calculation of flow near a spinning disc. Lett Heat Mass Transfer 1974;1:131–7.

[30] Crowe CT, Sharma MP, Stock DE. The particle-source-in cell (PSI-CELL) model for gas-droplet flows. J Fluids Eng 1977;99:325–32.

[31] Openfoam. http://www.openfoam.com. 2017.

Highlight

1. A Monte Carlo–based nongray radiation solver is developed to study effects of radiation in turbulent coal combustions.
2. Radiation significantly affects the lift-off height, flame shape, temperature fields, and species concentration fields in the target flame.
3. Radiation alters the heat transfer mechanism of particles from convection-dominant to radiation-dominant.
4. Nongray effects are found to be more important for gas phase than particle phase for the target flame.
5. The spectral properties of ash have insignificant influence on the present flame.